MR Elastography-based tissue stiffness in glioblastomas is associated with reduced cerebral blood flow

Author Names and Degrees: Siri Fløgstad Svensson[1,2], Elies Fuster-Garcia[1], Anna Latysheva[3], Jorunn Fraser-Green[4], Wibeke Nordhøy[1], Omar Isam Darwish[5], Ivar Thokle Hovden[1,2], Sverre Holm[2], Einar O. Vik-Mo[6], Ralph Sinkus[5,7], & Kyrre Eeg Emblem[1]

Author Affiliations: [1]Dept. of Diagnostic Physics, Oslo University Hospital, Oslo, Norway, [2]Department of Physics, University of Oslo, Oslo, Norway, [3]Department of Radiology, Oslo University Hospital, Oslo, Norway, [4]The Intervention Centre, Oslo University Hospital, Oslo, Norway, [5]Vilhelm Magnus Laboratory, Dept. of Neurosurgery, Oslo University Hospital, Oslo, Norway, [6]Division of Imaging Sciences and Biomedical Engineering, King's College, London, United Kingdom, [7]INSERM U1148, LVTS, University Paris Diderot, Paris, France

Corresponding Author Info: Siri F Svensson, { HYPERLINK "mailto:siriflo@uio.no" }, telephone: +47 916 05 269, Department for Diagnostic Physics, Building 20 Gaustad, Oslo University Hospital, PB 4959 Nydalen, 0424 Oslo, Norway

Grant Support: We gratefully acknowledge support from the European Union's Horizon 2020 Programme: ERC Grant Agreement No. 758657-ImPRESS, Research and Innovation Grant Agreements No. 668039-FORCE and Marie Skłodowska-Curie grant agreement (No 844646-GLIOHAB), South-Eastern Norway Regional Health Authority (Grant Agreement No. 2017073 and 2013069), The Research Council of Norway FRIPRO (Grant Agreement No. 261984), the National Institute of Health R21 grant (Grant Agreement No. EB030757), and the German Research Foundation (DFG, SCHR 1542/1-1).

Financial interest: KEE: NordicNeuroLab AS, Bergen, Norway – Intellectual property rights.

Abstract

BACKGROUND: Understanding how mechanical properties relate to functional changes in glioblastomas may help explain variation between patients.

PURPOSE: To map differences in biomechanical and functional properties between tumor and healthy tissue, to study their spatial distribution, and to assess any relationship between biomechanical and functional properties.

STUDY TYPE: Prospective.

SUBJECTS: Nine patients with glioblastoma, 17 healthy subjects

FIELDSTRENGTH/SEQUENCE: 3T, MRE, DSC, DTI, ASL

ASSESSMENT: Stiffness and viscosity measurements G′ and G″, cerebral blood flow (CBF), apparent diffusion coefficient (ADC) and fractional anisotropy (FA) were measured in patients' contrast-enhancing tumor, necrosis, edema, and gray and white matter, and in gray and white matter for healthy subjects.

STATISTICAL TESTS: Voxel-wise regression analysis using a linear and a random forest model for CBF as a function of ADC, FA, G′ and G″. Model performance was evaluated by root-mean-square error with a leave-one-patient-out cross-validation strategy. A paired Wilcoxon signed-rank test was used for comparisons of different regions and models. A significance level of $P<0.05$ was assumed for all tests.

RESULTS: Median G′ and G″ in contrast-enhancing tumor were 15 % and 39 % lower than in normal-appearing white matter (cNAWM), respectively ($P<0.01$). FA was 53 % lower in tumor compared to cNAWM ($P<0.01$). ADC and CBF were 50 % and 2.9 times higher in tumor than in cNAWM, respectively ($P<0.01$). For both models, prediction of CBF was improved by adding MRE measurements to the model, compared to a baseline model with ADC and FA as predictors ($P<0.05$).

DATA CONCLUSION: Tumors differed from healthy tissue with regard to G′ and G″, CBF, ADC and FA, with heterogeneity both between patients and within tumors. Measurements approached values in normal-appearing tissue when moving outward from the tumor core, but abnormal tissue properties were still present in regions of normal-appearing tissue. The inclusion of MRE measurements in statistical models helped predict perfusion, with stiffer tissue associated with lower perfusion values.

MR Elastography-based tissue stiffness in glioblastomas is associated with reduced cerebral blood flow

1 Introduction

Glioblastoma (GBM) is the most common primary malignant tumor in the central nervous system, and is usually rapidly fatal (1). With a standard treatment regimen of surgery and radiochemotherapy the median survival time is only 12-15 months (1).

Magnetic Resonance Imaging (MRI) is a crucial tool for diagnosing GBM and for measuring the effect of treatment. Perfusion and diffusion MRI are considered important methods for both understanding the tumor biology and for quantifying physiological processes (2). However, the changing biomechanical properties of a solid tumor and its surrounding tissue *in vivo* are less studied. Moreover, an understanding of how the mechanical properties of tissue relate to functional changes of perfusion and edema during cancer evolution, may help explain the substantial variation in appearance and treatment response between patients.

In this study, we use MR elastography (MRE) to measure biomechanical properties of GBM in combination with diffusion and perfusion imaging. MRE is a technique for non-invasively measuring the biomechanical properties of tissue (3). Earlier studies using MRE to examine patients with brain tumors have found that glioblastoma tumors differ from the healthy brain in terms of stiffness and viscosity (4-7). Most studies on MRE in brain tumors present mean values for the tumor stiffness and viscosity, yet glioblastomas display a large degree of heterogeneity, not only between patients, but also within the same tumor (8). Streitberger et al. noted that stiffness maps of glioblastomas were heterogeneous and composed of stiff and soft compartments. They hypothesize that the potential source of heterogeneity in $|G^*|$ may be that glioblastomas consist of both solid masses and possibly cystic and necrotic fractions (4). Furthermore, glioblastomas are known to infiltrate the surrounding tissue beyond the contrast-enhancing tumor, and this peritumoral area appears to play a key role in tumor growing and recurrence (9). The objective of our study is to map the differences between tumor and healthy tissue with regard to biomechanical and functional properties, to study their spatial distribution, and to assess any possible relationship between biomechanical and functional parameters. We segment tumors into contrast-enhancing and necrotic regions, and FLAIR-enhanced peritumoral edema region in order to study tumor heterogeneity and infiltration.

In data based on both patients with GBM and healthy subjects, we show that tumor tissue differs from healthy tissue in terms of both biomechanical properties, perfusion and diffusion. We find that with increased distance from the tumor core, the measurements approach values found in normal-appearing tissue. However, abnormal values for perfusion, diffusion and stiffness can still be found outside the areas labelled as normal-appearing on anatomical images, providing an insight into the infiltrative nature of glioblastoma. Finally, we model the relationship between the different measurements, and find that adding biomechanical parameters quantified via MRE improves the descriptive power of a model of cerebral blood flow as a function of the other parameters. All the data in our study is made publicly available through a public repository.

2 Material and methods

2.1 Acquisition

Data was collected from 9 patients with histopathologically confirmed glioblastoma, 4 females and 5 males, between 44 and 75 years (median 53 years). All tumors were IDH wildtype. In addition, 17 healthy subjects were scanned, 8 females and 9 males, between 21 and 34 years (median 25 years). All subjects signed an informed consent form. The study was approved by the National Research Ethics Committee and the institutional review board, and the examination was tolerated well by all patients and healthy subjects examined. Apart from the subjects included in the study, three healthy subjects and two patients were excluded due to inadequate MRE data quality.

The scans were performed on a 3T clinical MRI scanner (Ingenia, Philips Medical Systems, Best, the Netherlands) using a 32-channel head coil. Scan parameters for all sequences used are presented in **Table 1**. For the patients a T1-weighted ($T1_w$) anatomical reference scan was acquired both before and after (**Fig. 1A**) injection of a gadolinium-based contrast agent (Gadovist, Bayer Pharma AG, Germany), with a 0.1 mmol/kg body weight dose, followed by a 20 mL saline flush (BB. Melsungen AG, Melsungen, DE) (**Fig. 1H**). During contrast injection, 100 dynamic scans were acquired for perfusion imaging (10). For the DTI and DSC sequences, a pre-scan with the opposite phase-encoding direction was acquired to correct for echo-planar imaging (EPI) distortion in the image-processing pipeline (11). Perfusion imaging in healthy subjects was performed by a 2D pseudo-Continuous Arterial Spin Labelling sequence (12).

In MRE, a vibrational device is used to cause oscillating shear displacements of tissue (13). Here, we used a gravitational transducer (14) attached on the side of the subject's head to induce shear waves of 50 Hz into the brain. The scan duration was 5.5 minutes. Further details about the MRE acquisition can be found in (15).

Sequence	TR [ms]	TE [ms]	Acquisition matrix	Resolution [mm^3]	Additional information	Used for
T_{2w}	3000	80	420×270×28	0.6×0.6×4	Turbo-SE sequence	Patients
FLAIR	4800	320	252×249×183	1×1×1	Turbo-SE sequence, inversion time=1650 ms	Patients
DSC GRE-SE	1500	25 (GRE)/ 105 (SE)	100×125×11	1.8×1.8×5	Combined single-shot 2D GRE-SE, SENSE 2, EPI readout	Patients
T_{1w}	5.2	2.3	256×256×368	1×1×1	3D inversion recovery turbo field echo, flip angle=8°, shot interval=3000 ms, inversion delay= 853 ms	All subjects
DTI	9800	60	94×94×50	2.5×2.5×2.5	SE, single-shot, EPI readout, SENSE-factor 2, 15 gradient directions, b-values 0 s/mm^2 and 800 s/mm^2	All subjects
MRE	295	12	72 × 70 × 15	3.1×3.1×3.1	MEG strength 13.2 mT/m, SENSE-factor 2	All subjects
ASL	4400	14.8	72 × 70 × 15	3.6×3.6×5.5	2D pCASL, labelling duration 1.8 s, post-label delay 1.8 s, 35 pairs of label and control volumes, EPI readout	Healthy subjects
PD	12000	12	72 × 70 × 15	3.6×3.6×5.5	Used for calibration of the subtracted and averaged ASL images	Healthy subjects

Table 1: Scan parameters. *Scan parameters used in the different MRI sequences. Abbreviations: T2-weighted (T_{2w}), T1-weighted (T_{1w}), Dynamic susceptibility contrast (DSC), gradient-echo (GRE), spin-echo (SE), echo-planar imaging (EPI), sensitivity encoding (SENSE), Diffusion tensor imaging (DTI), MR Elastography (MRE), Arterial Spin Labelling (ASL), pseudo-Continuous Arterial Spin Labelling (pCASL), Proton-density weighted (PD).*

2.2 Image processing

From the MR acquisitions described above, we constructed perfusion, diffusion and elastography images. Details about image processing and registration can be found in Supplementary information. Figure 1 shows maps of cerebral blood flow (CBF) **(Fig. 1B,I)**, apparent diffusion coefficient (ADC) **(Fig. 1C,J)**, and fractional anisotropy index (FA) **(Fig. 1D,K)** for both patients and healthy subjects**.** MRE parameters used are the shear storage modulus G′ (as a measure for stiffness) and the shear loss modulus G″ (related to the viscosity, meaning the tissue's ability to dissipate energy) (**Fig. 1E-F, L-M**).

Patient data was segmented into contrast-enhancing tumor, edema, necrosis, and normal-appearing gray and white matter (**Fig. 1N**). Data from healthy subjects was segmented into gray and white matter. Gray matter was further subdivided into the deep gray and cortical matter regions. Deep gray matter regions included in the study were head of the caudate nucleus, putamen, thalamus and hippocampus. The cortical gray matter regions included were the frontal lobe, the occipital lobe, the parietal lobe and the temporal lobe. (**Fig. 1G**).

In addition to measuring absolute values, we also normalized elastography and diffusion measurements in gray matter regions to the mean value in each subject's white matter.

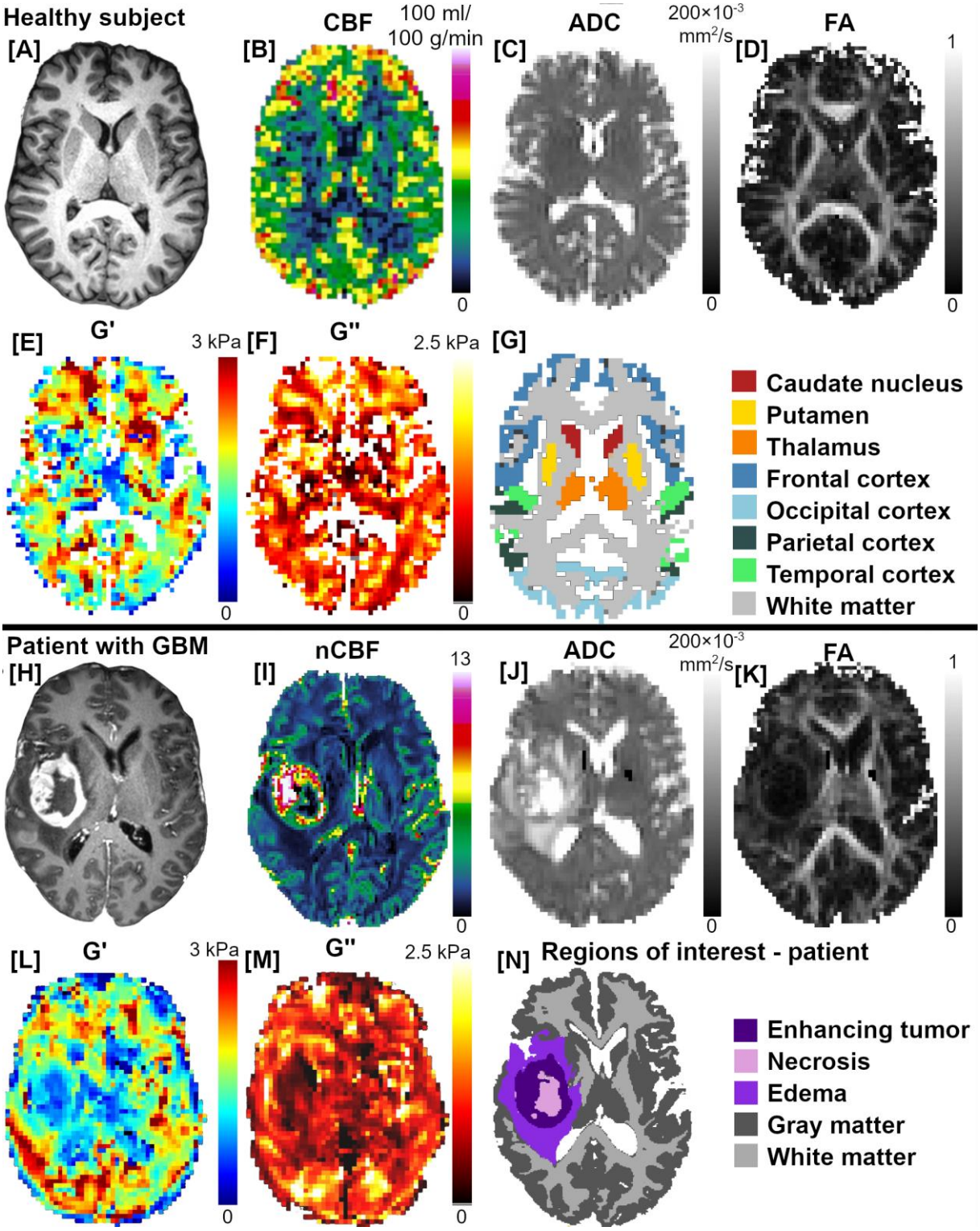

Figure 1: Biomechanical and functional maps in healthy subjects and patients. *A) Anatomical T1-weighted ($T1_w$) image, B) cerebral blood flow (CBF), C) apparent diffusion coefficient (ADC), D) fractional anisotropy index (FA) E) storage modulus G', and F) loss modulus G'', maps shown for a healthy 24-year-old male subject. G) shows the regions of interest used for the healthy subjects, except from hippocampus, which is not visible in this*

slice. Pre-surgical, H) contrast-enhanced $T1_w$ image, I) normalized CBF, J) ADC, K) FA, L) G′, M) G″ maps for a 50-year-old female subject with glioblastoma. N) shows contrast-enhancing tumor, necrosis, edema, and normal-appearing gray and white matter regions of interest.

2.3 Statistics

For each individual, we computed the mean value of each parameter in all regions of interest (ROIs). In the results below, we present the median of these mean values across individuals, with the range for each parameter in parenthesis. A comparison of measurements in different regions was done by a paired Wilcoxon signed-rank test. A Spearman rank correlation test was used to assess the relationship between the different parameters for the mean values in each ROI.

To visualize each tissue's signature across diffusion and MRE parameters, the mean measurements in each region for each patient and healthy subject was dimensionally reduced using t-distributed stochastic neighbour embedding (t-SNE).

Voxel-wise regression analysis in MNI space was performed using both a simple linear model and a random forest model for perfusion as a function of ADC, FA, G′ and G″. The performance of the regression models was evaluated by their root-mean-square error (RMSE) with a leave-one-patient-out cross-validation strategy. The different models were compared using a paired Wilcoxon signed-rank test.

A significance level of $P<0.05$ was assumed for all tests, after Holm-Bonferroni corrections for multiple comparisons. All statistical analyses were done using Matlab.

3 Results

Glioblastoma tissue is structurally degraded compared to healthy tissue

The results of the measurements in the different regions of interest defined for the GBM patients and for the healthy subjects are summarized in **Table 2**.

PATIENTS	Median G′ [kPa] (range)	Median G″ [kPa] (range)	Median G′ norm (range)	Median G″ norm (range)	Median ADC [10^{-3} mm^2/s] (range)	Median FA (range)	Median nCBF (range)
Contrast-enhancing tumor	1.38 (1.15-1.62)	0.65 (0.55-0.80)	0.85 (0.70-1.02)	0.64 (0.51-0.73)	1.22 (1.01-1.47)	0.19 (0.14-0.25)	3.70 (2.98-9.64)
Necrotic region	1.19 (0.70-1.76)	0.61 (0.37-0.81)	0.69 (0.50-1.11)	0.62 (0.40-0.74)	1.37 (0.94-1.90)	0.10 (0.09-0.16)	2.11 (1.48-3.61)
Edema	1.62 (1.53-2.16)	0.87 (0.68-1.09)	1.01 (0.86-1.33)	0.88 (0.66-1.03)	1.27 (1.01-1.47)	0.20 (0.16-0.34)	1.57 (0.97-2.46)
Average gray matter	1.66 (1.34-1.73)	1.02 (0.90-1.16)	1.02 (0.87-1.07)	0.99 (0.91-1.09)	0.91 (0.85-1.08)	0.16 (0.14-0.17)	2.42 (2.06-2.94)
Average white matter	1.62 (1.36-1.90)	1.06 (0.91-1.23)	-	-	0.81 (0.77-0.89)	0.39 (0.34-0.43)	1.27 (1.11-1.45)
HEALTHY SUBJECTS	**Median G′ [kPa] (range)**	**Median G″ [kPa] (range)**	**Median G′ norm (range)**	**Median G″ norm (range)**	**Median ADC [10^{-3} mm^2/s] (range)**	**Median FA (range)**	**Median CBF [ml/100 g/min] (range)**
Caudate nucleus	1.49 (1.25-1.83)	0.84 (0.45-1.15)	0.82 (0.71-1.00)	0.72 (0.40-0.95)	0.74 (0.70-0.81)	0.22 (0.18-0.24)	20 (7-35)
Hippocampus	1.83 (1.30-2.31)	0.96 (0.72-1.14)	1.01 (0.76-1.22)	0.80 (0.59-0.93)	0.88 (0.83-0.93)	0.18 (0.16-0.23)	20 (8-31)
Putamen	1.78 (1.46-2.16)	1.11 (0.77-1.58)	0.96 (0.83-1.17)	0.91 (0.70-1.33)	0.73 (0.71-0.76)	0.20 (0.17-0.23)	24 (12-37)
Thalamus	1.40 (1.21-1.55)	0.73 (0.50-1.03)	0.76 (0.65-0.88)	0.60 (0.46-0.80)	0.80 (0.76-0.84)	0.29 (0.27-0.30)	24 (12-44)
Frontal lobe	1.65 (1.39-1.90)	1.14 (0.88-1.33)	0.91 (0.76-1.10)	0.94 (0.76-1.09)	0.88 (0.86-0.91)	0.17 (0.15-0.18)	44 (23-71)
Occipital lobe	1.44 (1.11-2.15)	1.17 (0.89-1.39)	0.78 (0.61-1.20)	1.01 (0.70-1.26)	0.85 (0.83-0.87)	0.16 (0.15-0.18)	40 (25-62)
Parietal lobe	1.74 (1.38-2.55)	1.23 (0.96-1.35)	0.95 (0.75-1.30)	1.01 (0.81-1.16)	0.86 (0.84-0.88)	0.16 (0.15-0.18)	40 (20-68)
Temporal lobe	1.81 (1.55-2.28)	1.32 (1.18-1.63)	1.00 (0.81-1.23)	1.10 (0.95-1.45)	0.87 (0.85-0.89)	0.16 (0.15-0.17)	36 (21-60)
Average gray matter	1.68 (1.48-1.97)	1.16 (1.01-1.23)	0.89 (0.81-1.07)	0.97 (0.85-1.09)	0.86 (0.85-0.88)	0.17 (0.16-0.18)	40 (22-62)
Average white matter	1.84 (1.70-1.96)	1.19 (1.10-1.32)	-	-	0.80 (0.77-0.82)	0.33 (0.32-0.37)	NA

Table 2: Measurements in patients (n=9) and healthy subjects (n=17): *The upper part of the table shows measurements in patients: median values (range) of storage modulus G′, loss modulus G″, diffusivity ADC, fractional anisotropy and normalized cerebral blood flow nCBF (as measured by DSC MRI) are presented, measured in contrast-enhancing tumor, edema and necrosis, and normal-appearing contralateral white and gray matter. The lower part of the table shows corresponding measurements in regions-of-interest in healthy subjects. Note that CBF measurements in healthy subjects were acquired using ASL MRI in absolute units, and are not directly comparable to CBF measurements in patients, which needs to be normalized (nCBF) to be considered quantitative. MRE measurements* G'_{norm} *and* G''_{norm} *normalized to each subject's normal-appearing contralateral white matter are also presented.*

The median value of the G′ in the contrast-enhancing tumor was 15 % lower than in contralateral normal-appearing white matter (cNAWM) (P<0.01). G″ was 39 % lower in contrast-enhancing tumor than in white matter (P<0.01). FA was also lower in tumor compared to white matter, with a 53 % reduction (P<0.01). ADC, however, was 50 % higher in tumor than in white matter (P<0.01), and CBF was 2.9 times higher in contrast-enhancing tumor than in white matter (P<0.01). Especially CBF showed a large variability between patients, with the

highest patient mean CBF in contrast-enhancing tumor 3.2 times higher than the lowest value of mean CBF for a patient.

In the edema surrounding the tumor, median G′ was similar to cNAWM (P=0.6), while G″ was 18 % lower in edema than in white matter (P<0.05). FA was 48 % lower in edema compared to white matter (P<0.05). ADC was 56 % higher in edema than in white matter (P<0.01), while CBF was 24 % lower in edema than in white matter (P<0.01). **Figure 2** illustrates the combinations of biomechanical and functional parameters in the different tumor regions and for healthy regions.

Tumor stiffness is heterogeneous, both among patients and within tumor

The mean values of G′ and G″ showed a tendency to be lower in necrosis than in contrast-enhancing tumor (P=0.06 and P=0.07, respectively). This suggests a heterogeneity within-tumor, illustrated in **Figure 3**: The G'_{norm} and G''_{norm} voxels distributions for each patient differed in contrast-enhancing tumor, necrosis and edema. The differences between patients were also larger in these pathological regions than in normal-appearing gray matter, illustrating the tumor heterogeneity between patients.

This variability is also illustrated in **Figure 4**, which shows the distribution of G′, G″, ADC and FA among healthy subjects and patients. The measurements in the tumor and the edema showed a larger inter-patient variability than the values in patient white and gray matter.

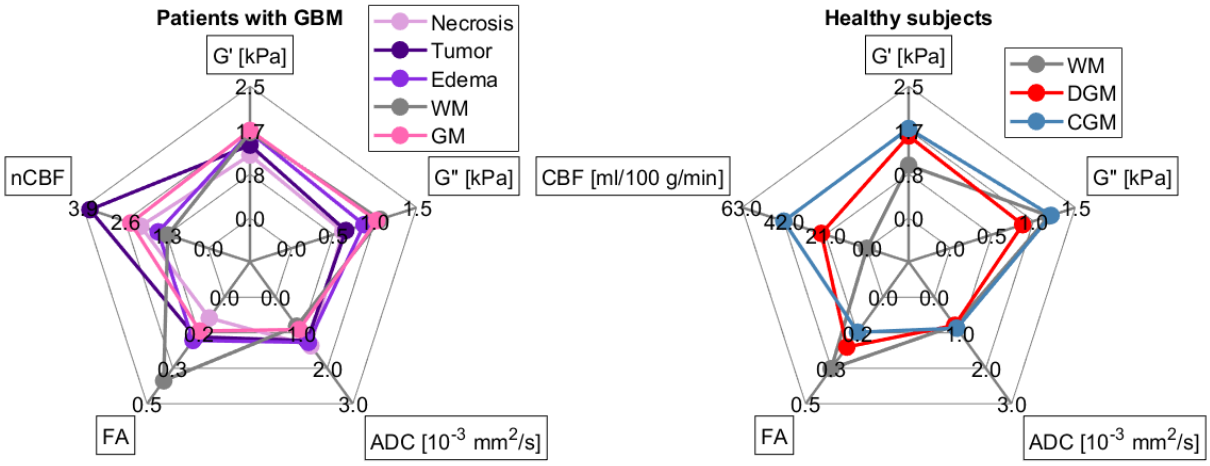

Figure 2: Spider plots of the different parameters in patients and healthy subjects*. Median values of G', G'', ADC, FA and CBF shown in the necrotic region, contrast-enhancing tumor, edema, white and gray matter in patients (left) and in white, deep gray and deep cortical gray matter in healthy subjects (right).*

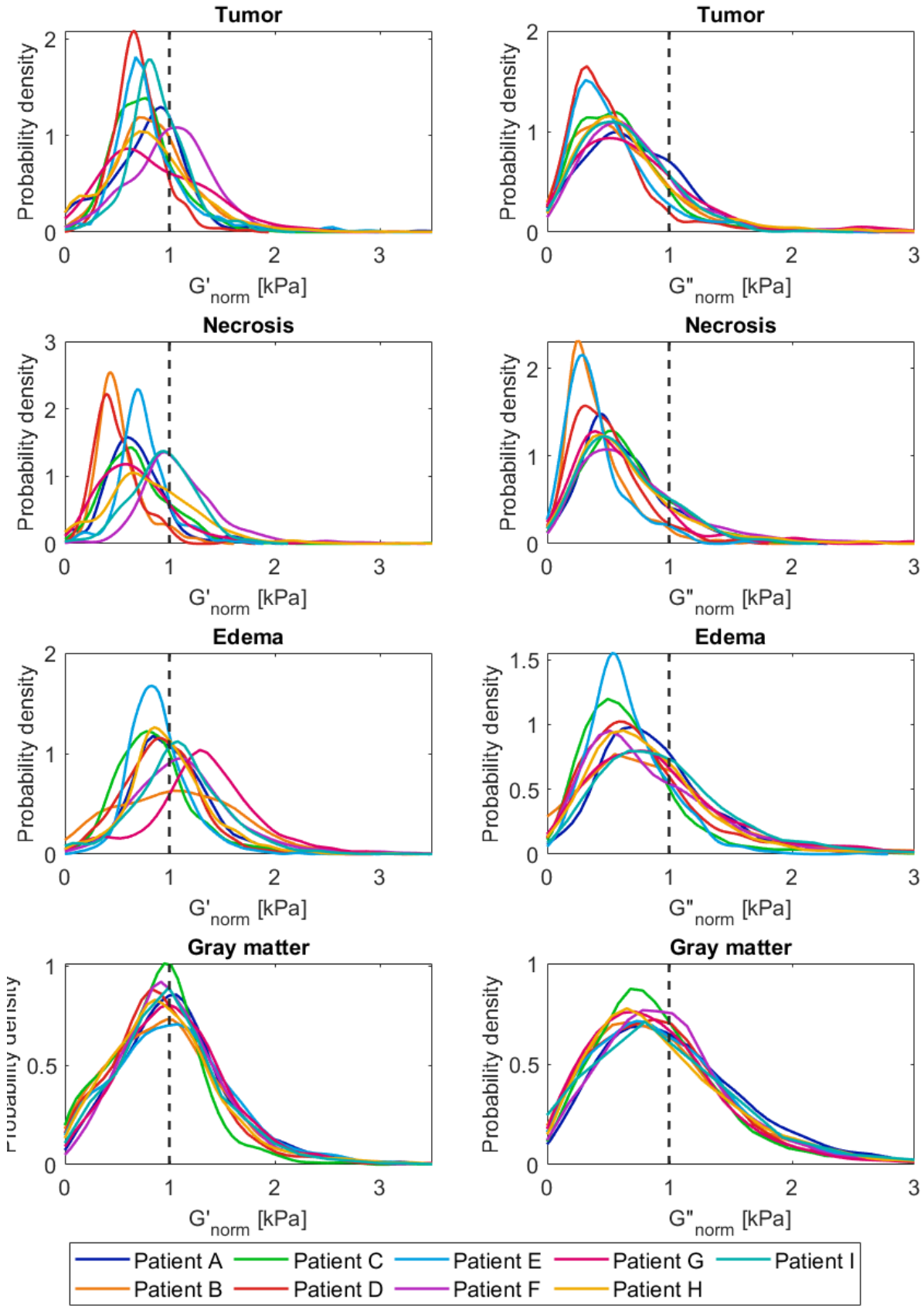

Figure 3: Distribution of biomechanical properties in different tumor regions and gray matter. *Plot shows distribution of voxel values for G'_{norm} and G''_{norm} in contrast-enhancing tumor, necrosis, edema and normal-appearing gray matter. The distribution for each patient differs in the different parts of the lesion, illustrating intra-patient heterogeneity of stiffness and*

viscosity. The lesion distributions also differ more between patients than the distributions for gray matter, illustrating the inter-patient heterogeneity.

Patient normal-appearing white matter shows lower stiffness, viscosity and anisotropy than white matter in healthy subjects

The white matter region in patients had 12 % lower G′ ($P<0.05$) and 11 % lower G″ ($P<0.01$) measurements compared to the white matter region in healthy subjects. FA, on the other hand, was 17 % higher than in the healthy subjects ($P<0.001$). ADC was similar in healthy and patient white matter ($P=0.1$). CBF between patients and healthy subjects were not compared as they were acquired from different techniques.

Figure 4 shows the distribution of the different measurements in each region, for both healthy subjects and patients. For the healthy subjects, G′ was 9 % higher in cortical gray matter compared to that of deep gray matter ($P<0.01$). G″ was 39 % higher in the cortical gray matter compared to that of deep gray matter ($P<0.001$).

Comparing white matter to deep gray matter, G′ was 18% higher in white matter ($P<0.01$), while G″ was 37 % higher in white matter than ($P<0.001$). G″ was similar in white and cortical gray matter ($P=0.99$).

The median CBF was 83% higher in the cortical gray matter than in deep gray matter ($P<0.001$). ADC was 11 % higher in cortical than in deep gray matter ($P<0.001$), and 9 % lower in white than in cortical gray matter ($P<0.05$). The FA was 30 % lower in cortical gray matter than in deep gray matter ($P<0.001$), 43 % higher in white matter than deep gray matter ($P<0.001$), and 204 % higher in white matter than cortical gray matter ($P<0.001$).

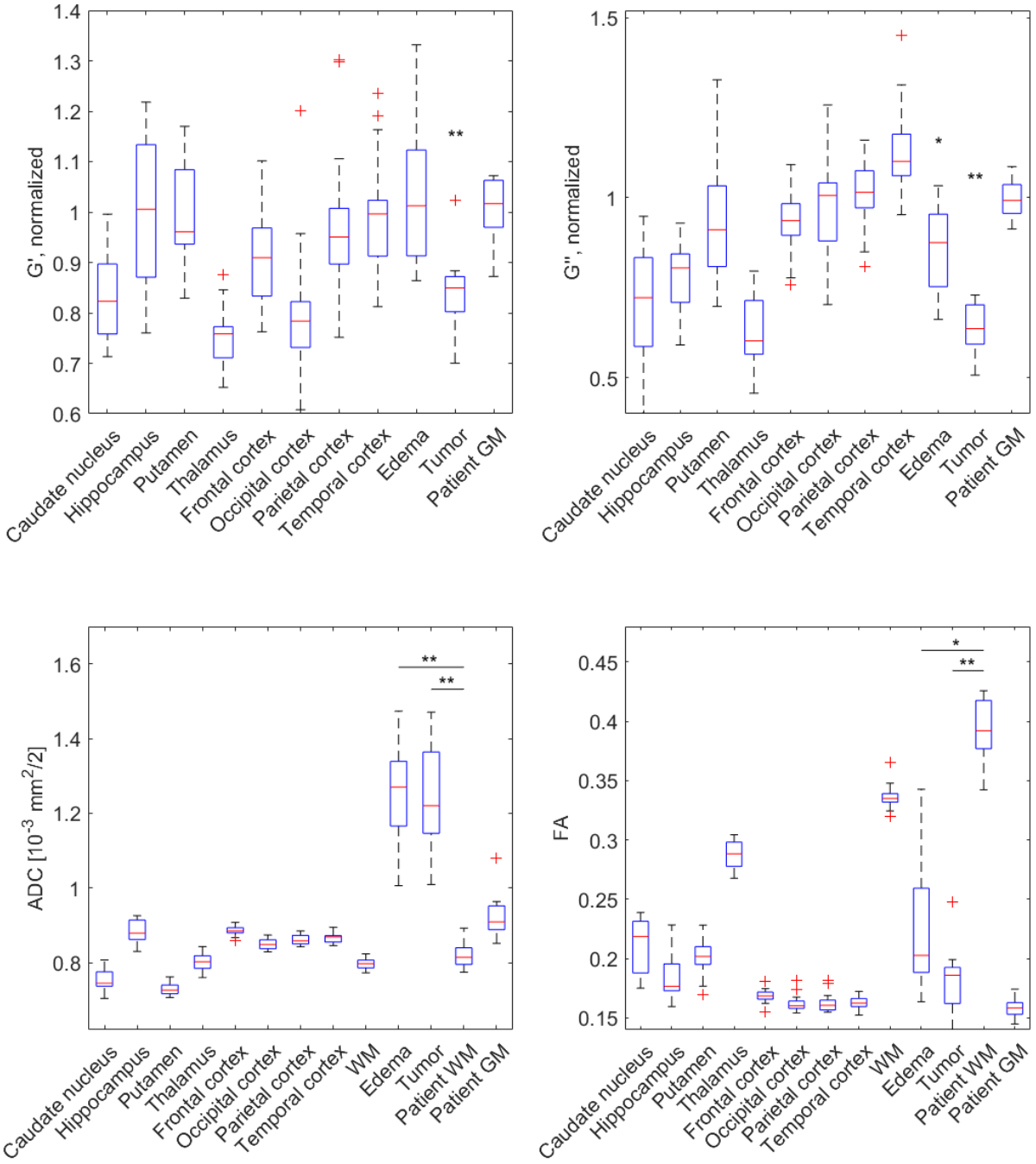

Figure 4: Parameter distributions in healthy brain regions vs tumors. *Box plots for A) storage modulus G′ normalized to white matter, B) loss modulus G″ normalized to white matter, C) apparent diffusion coefficient (ADC), and D) fractional anisotropy (FA) for all ROIs in healthy subjects and in edema, contrast-enhancing tumor, white and gray matter in patients. The box plots show the median value (red line) and the 25th and 75th percentile (blue box) of the mean values in the different regions for the 17 healthy subjects and the 9 patients. Asterisk show significant differences from patient's contralateral normal-appearing white matter, with *=P <0.05, **=P<0.01. The measurements in the tumor and the edema showed a larger inter-patient variability than the values in patient white and gray matter.*

The t-SNE plot (**Fig. 5**) illustrates the separation of the different brain regions in both patients and healthy subjects, for ADC, FA, G′ and G″. Most regions of interest in healthy subjects tracked together, and showed a separation between deep and cortical gray matter regions. The

contrast-enhancing tumor, edema and necrosis were close to each other and separated from the healthy ROIs.

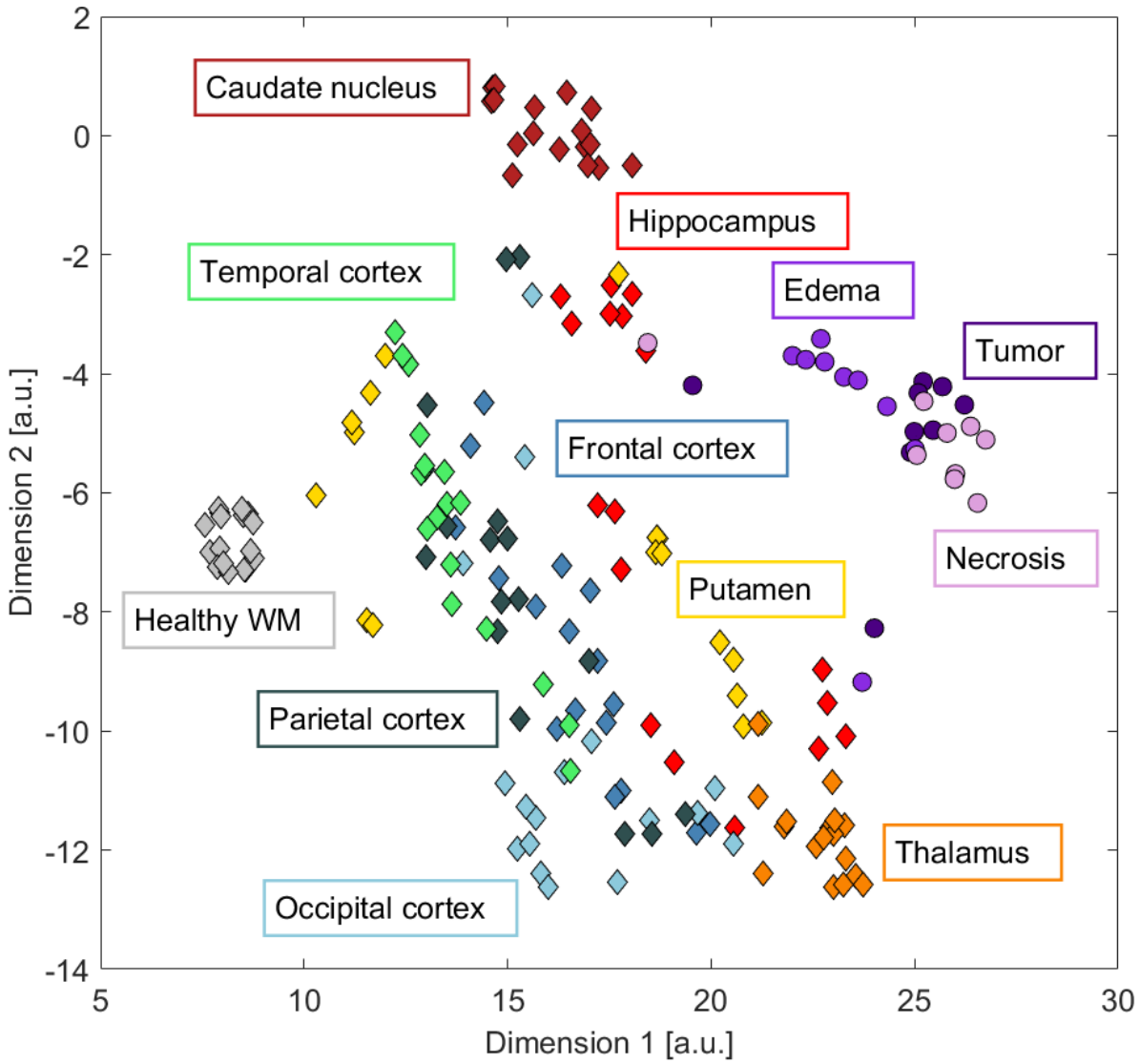

Figure 5: Brain regions in healthy subjects and patients with ADC, FA, G'_{norm} and G''_{norm} reduced into two dimensions. *This visualization shows the mean measurements of each region for all healthy subjects and patients using t-distributed stochastic neighbour embedding, with arbitrary units (a.u) on axes. Pathological regions group together away from healthy tissue. Diamond markers correspond to measurements in healthy subjects, circles to patients. WM: white matter, GM: gray matter.*

Tissue properties approach normal values further away from tumor core

Figure 6 illustrates the values in the necrotic and contrast-enhancing tumor and edema, moving radially out from the tumor core. G′ and G″ started from low values within the tumor and increased toward values found in cNAWM at the distal edge of the edema region. ADC was high for necrosis, tumor and edema, and was still 30 % (median value) higher than in cNAWM at the edema edge—although with large variation among patients. FA was also low in the center of the tumor and increased away from the tumor core; the median value was 47 % lower than

in normal-appearing matter at the edge of the edema. CBF, leakage and vessel size were highest in the contrast-enhancing tumor, and gradually decreased toward the mean value in cNAWM at the edge of the edema.

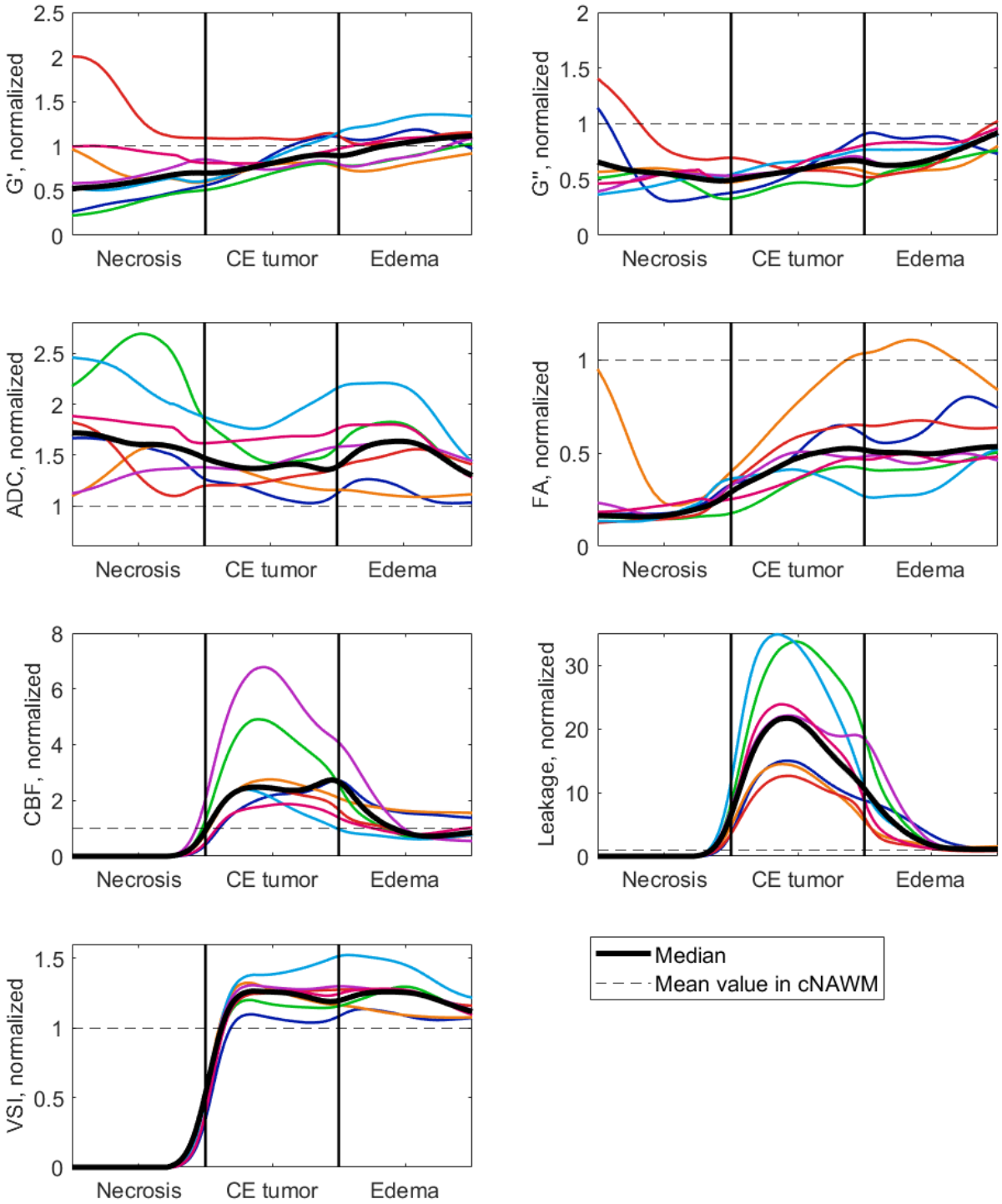

Figure 6: Gradients of the different parameters in the lesion. *This figure shows gradients of the different parameters, normalized to mean value in contralateral normal-appearing white matter, moving radially out from the tumor core, through necrosis, contrast-enhancing tumor and edema. All distances were normalized to the maximum distances between necrotic core and contrast-enhancing tumor, inner contrast-enhancing tumor and edema, inner edema and edge to normal-appearing matter, respectively. Colored lines show individual patients (n=7) and the*

black line shows the median value for all patients. At the outer edge of the edema, most values approached mean values in normal-appearing white matter, shown by the dotted line. Abbreviation: Vessel size index (VSI).

Tissue may have abnormal properties outside lesion area

Figure 7 illustrates the gradients of the different parameters moving radially outward from the lesion, defined as any necrotic, contrast-enhancing or edematous regions. This was tissue that appeared normal on the anatomical images and was not labelled as tumor. However, for several of the patients, the properties of the tissue remained abnormal (outside the 25th and 75th percentile of cNAWM) for more than 10 mm into the normal-appearing tissue. 3/7 patients had abnormal G″ values > 10 mm outside the lesion edge, while two different patients showed abnormal values for ADC and FA > 10 mm outside the lesion edge, respectively.

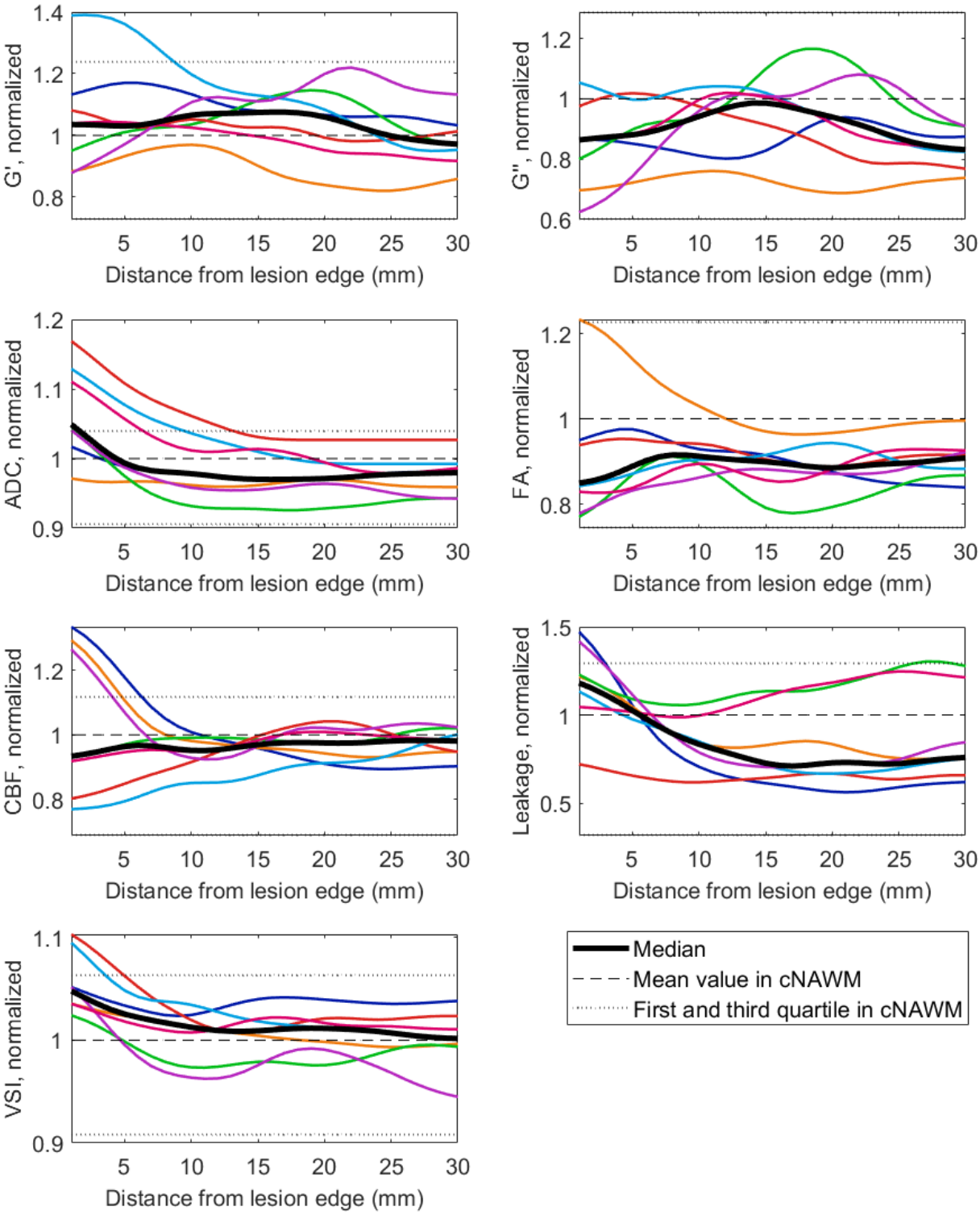

Figure 7: Gradients of the different parameters moving radially outwards from the lesion edge. *Measurements in matter labelled as white matter, normalized to each patient's average value in contralateral normal-appearing white matter (cNAWM). Colored lines show individual patient gradients (n=7), black line shows median values for all patients. Dashed line indicates the mean value in cNAWM, dotted lines the 25th and 75th percentiles of the cNAWM. For some patients, biomechanical and functional parameters remained abnormal past 10 mm into normal-appearing tissue outside the lesion. Abbreviation: Vessel size index (VSI).*

High cerebral blood flow related to low stiffness

No correlations across patients were found in the contrast-enhancing tumor between mean G′ and mean CBF, ADC, leakage or vessel size, nor between G″ and the perfusion and diffusion parameters. The same was true for edema, and normal-appearing gray and white matter. For the healthy subjects, the only correlation between parameters was between G′ and G″ in gray ($P<0.01$) and white matter ($P<0.01$).

We estimated voxel-by-voxel regressions to explain CBF as a function of our measurements, which where all were normalized to cNAWM. Our baseline model was a linear model with ADC_{norm} and FA_{norm} as predictors. Using RMSE as a criterion, we then investigated how predictive power increased as we added first G'_{norm} and then both G'_{norm} and G''_{norm} to the model. Results are presented in **Table 3**, column 1. We found that predictive power increased significantly with the inclusion of each additional predictor. After the assessment of each model, the linear model was trained using all data, and the final linear model is $CBF= 1.8 - 0.23 \cdot G'_{norm} - 0.16 \cdot G'_{norm} + 0.35 \cdot ADC - 0.51 \cdot FA$.

In addition to the linear model, we investigated the predictive ability of a random-forest model. Results are presented in Table 3, column 2. Again, we compare a baseline model including ADC_{norm} and FA_{norm} to models including G'_{norm} and both G'_{norm} and G''_{norm}. All three random-forest models performed significantly better than the linear models ($P<0.01$). In addition, the performance of the random forest model improved by including G'_{norm} ($P<0.01$), and further improved by including both G'_{norm} and G''_{norm} ($P<0.01$).

	Linear model	**Random forest**
CBF_{norm} as a function of ADC_{norm}, FA_{norm}	0.857 (0.831-0.865)	0.680 (0.657-0.685)
CBF_{norm} as a function of ADC_{norm}, FA_{norm}, G_{norm}'	0.852 (0.826-0.860) *	0.656 (0.634-0.662) **
CBF_{norm} as a function of ADC_{norm}, FA_{norm}, G'_{norm}, G''_{norm}	0.849 (0.824-0.858) *	0.607 (0.586-0.612) **

Table 3: Performance of models predicting CBF_{norm} as a function of the other parameters.: *Median root-mean-square errors (range) for a linear model and a random forest model using only diffusion parameters to predict CBF normalized to contralateral normal-appearing white matter (CBF_{norm}) in patients (upper row), versus including the G'_{norm} parameter from MRE (middle row) and both G'_{norm} and G''_{norm} (lower row). Asterisk indicates significant improvement from the row above. Including G'_{norm} improved the model performance compared to only diffusion parameters ($P<0.05$), and including G''_{norm} as well further improved the performance ($P<0.05$). The random-forest model improved performance compared to the linear model ($P<0.01$).*

Data accessibility

All the data and the associated meta-data generated as a part of this study is publicly available by request through Zenodo (10.5281/zenodo.4926005).

4 Discussion

In this study, we used MR elastography, perfusion and diffusion imaging to measure the biomechanical and functional properties of different regions of the brain in patients with glioblastoma and in healthy individuals. We found that glioblastoma tissue was structurally

degraded compared to healthy tissue in terms of all measured parameters. In addition, although measurements approached normal values when moving away from the tumor core, we found abnormal tissue properties in regions that appear normal on anatomical images. Finally, we used our measurements to construct a predictive model for CBF, which showed that perfusion increased with decreased G′ and G″.

Stiffness and viscosity in tumors, here measured by the storage and loss shear modulus (G′ and G″, respectively), were significantly lower than in the patients' contralateral normal-appearing white matter. This is consistent with previous reports from MRE in patients with brain cancer: Gliomas have been found to be softer than normal tissue (4,6,7,16) and substantially less viscous (4,5,7). In our study, we found G′ to be 15 % lower in tumor than in normal-appearing white matter, while G″ was reduced by 39 %. A reduction in both G″ and G′ can be interpreted as a softening of the mechanical rigidity of the tissue. A decrease of the ratio between the two, such as when G″ is reduced more than G′, indicates that the material turns more springlike. Some research groups propose to interpret this change in phase angle as a reduction of the complexity of the tissue architecture and degradation of the tissue (17). However, this remains to be shown on the molecular level.

Most earlier studies of MRE in glioblastomas have presented mean tumor values. In our study, the tumors were segmented into contrast-enhancing and necrotic regions. We found the distribution of stiffness and viscosity to differ more in the tumors than in normal-appearing matter, and with a tendency for necrotic regions to be have even lower stiffness and viscosity than the contrast-enhancing parts of the tumor. In a longitudinal study of MRE in mouse-model gliomas, Schregel et al. found that tumors became softer and more heterogeneous over time with tumor progression and that softer sub-regions of the tumor were characterised by a high heterogeneity (18).

Our results related to FA, ADC, and CBF are consistent with previous findings in the literature. We observed lower values of FA in the tumor, edema, and necrotic regions relative to normal-appearing matter. This is because glioma infiltration disrupts the organization of white matter tracts, which is reflected in a reduction in FA With respect to ADC, we found high values in the edematous and necrotic regions, suggesting the presence of unrestricted water movement (19). Finally, our results showed high cerebral blood flow in the tumor compared to normal issue. As a new tumor grows, new vascular structures are formed to nourish the growing tumor. These immature vessels are leaky and structurally abnormal, which may cause high local tissue blood volume and irregular blood flow (19). Moreover, our CBF results also illustrate the interpatient heterogeneity: the patient with the most vascularized tumor had three times higher normalized CBF in the contrast-enhancing tumor compared to the least vascularized tumor.

Tumors and healthy tissue displayed distinct characteristics. Using a two-dimensional projection, we have shown how regions of interest in the healthy subjects tracked together, while the tumor components were grouped together as a separate cluster. The tumors were characterised by lower stiffness, viscosity and anisotropy than healthy tissue, while diffusivity was higher.

Areas displaying high signal on FLAIR images is presumed to represent edema due to cancer infiltration, and these regions are considered important elements of treatment planning (9). We calculated radial gradients passing through the contrast-enhancing tumor and the peritumoral tissue and further out to assumed healthy tissue. We found that tissue properties in edema had different characteristics than contralateral healthy tissue, but that the properties approached

those of healthy tissue further out in the edema, which is illustrative of the tumors' infiltrative character (20). For some patients, abnormal tissue measurements were also found even further away from the tumor core, in regions appearing normal on anatomical scans, implying that infiltration may extend beyond the increased FLAIR signal. Further studies including more patients is warranted to learn more about the differences between patients.

No evidence of association between the mean values of the different parameters measured on a full region level in patients was found as measured by a Spearman's rank correlation. The lack of correlation at the region level may be due to a small sample size and low power; it may also be due to spatial variation of biomechanical and functional properties within regions. If we expect the tissue perfusion to depend on diffusion and stiffness properties, such a relationship would depend on the spatial distribution of the tumor and surrounding tissue, due to the GBM heterogeneity. Therefore, all voxels for all patients were considered when making a regression model of perfusion as a function of the diffusion parameters, and the effect of including MRE parameters in the model was investigated. Even for a simple linear model, MRE added to the performance of the model, suggesting that MRE provides independent data. Biomechanical properties of the tissue may play an integral role in explaining the vascularity of the tumor. The simple linear model showed that CBF increased when G' and G'' decreased, an effect that could possibly be caused by vessels being compressed by stiff tissue and hence reduced perfusion (21). Of course, there might be a more complex relationship between various characteristics. Other studies have found that tumor stiffness may be affected by factors such as increased cellularity, increased vessel density, and interstitial fluid pressure (6). A study using MRE to study tumor growth in mice suggests that the tissue stiffness is influenced by the architecture of the blood vessels, rather than their state of perfusion (22). Further work is warranted to corroborate our findings.

The stiffness and viscosity of the contralateral normal-appearing white matter in the patients differed significantly from the measurements in white matter in the healthy subjects. Earlier studies have found brain stiffness to decrease with age (23). One study found that the decrease in stiffness (defined as the product of wave speed squared and tissue density) varied with brain region, ranging from -0.014 ± 0.002 kPa/year in the temporal lobe to nonsignificant in deep gray and white matter (24). Takamura et al. found that the largest decrease in stiffness, as measured by $|G^*| = \sqrt{G'^2 + G''^2}$, was in the sensorimotor areas, with -0.0136±0.0016 kPa/year, and -0.008±0.0025 kPa/year in the deep gray and white matter regions (25). The median age of the healthy subjects in our study was 25, and the median age of the patients was 53 years. The difference between the median white matter G' between patients and healthy subjects was 0.22 kPa, corresponding to -0.008 kPa/year (range 0.002-0.012 kPa/year). Although the studies mentioned here used other measurements of stiffness, the amount of change is roughly comparable between studies, and can explain the differences in the two study populations. Normalizing measured values to values in normal-appearing white matter is typically done in MRE studies of brain cancer patients (4,5,16). Such a within-patient normalization can also remove confounding effects in the case of different MRE acquisition techniques for reconstructed stiffness and viscosity values (26).

For patients, the brain was segmented in contrast-enhancing and necrotic tumor, edema, and normal-appearing gray and white matter. Our study focused on the differences between pathological and healthy tissue. For healthy subjects, we further subdivided the gray matter regions to compare with earlier studies of MRE in the healthy brain. We found white matter to be stiffer than gray matter, consistent with earlier published results of MRE in the healthy brain

(13). We found cortical gray matter to be stiffer than deep gray matter. This is in contrast to a recent study in 134 healthy subjects, where deep gray matter was reported to be stiffer than both white and cortical gray matter (27). A second study reported the stiffness to be lower in the deep gray matter than white matter (28), while a third study found white and gray matter stiffness to be very similar in both adults and paediatric subjects. This last study also noted a data quality bias in the calculations due the attenuation of the applied shear waves causing low MRE signal in the central regions of the brain (29,30). In an earlier study using this MRE method in healthy subjects, MRE data quality, measured as the curl-divergence ratio, was found to be lower in the deep gray matter regions than in regions closer to the skull. The study found no significant correlation between this data quality and stiffness measurements (15). The existing studies differ with respect to both MRE hardware and reconstruction methods. This makes it challenging to conclude about the reasons for discrepancies between studies.

A general challenge for MR elastography is the lack of a gold standard for *in vivo* tissue stiffness measurements. A specific challenge for our study, is the limited sample size, especially for patient data.

We expect some partial-volume effects with our current image resolution. This might contribute to less precise measurements in small regions and thin structures such as the cerebral cortex. To avoid interpolation effects due to low resolution, the MRE, diffusion and perfusion data were all analysed in their native spaces for the calculation of mean values. To ensure statistical validity, we only included regions with > 80 voxels in our analysis. To reduce contributions from cerebrospinal fluid, the healthy subject ROIs were also masked using an ADC cutoff value.

Different techniques were used in perfusion imaging of healthy subjects and patients. This hindered direct comparisons between the two groups in terms of perfusion. ASL was employed as the perfusion technique in healthy subjects as it is non-invasive, in contrast to DSC, where a gadolinium-based contrast agent is administered intravenously. In a potential future study comparing MRE and perfusion in both patients and healthy subjects, ASL could be used for all participants, and could be improved by employing a state-of-the-art 3D ASL sequence. No pre-scan with opposite phase was acquired prior to the ASL scan, so EPI distortion artifacts may have contributed to less precise coregistration to the anatomical labels, possibly biasing CBF measurements in healthy subjects (31).

The repeatability, assessed as the coefficient of variation, has been measured to be 4 % for the employed MRE technique (15). This should be taken into account if comparing small stiffness differences between subjects or longitudinal tracking over time.

Conclusion

We have characterized the brain tissue of patients with glioblastoma and healthy subjects using MR Elastography, perfusion and diffusion imaging. We found that the tumors differed from healthy tissue in terms of the biomechanical properties G' and G'', cerebral blood flow, diffusivity and fractional anisotropy, with heterogeneity both between patients and within tumors. Measurements approached values in normal-appearing tissue when moving outward from the tumor core, but abnormal tissue properties were still present in regions appearing normal on anatomical images. Finally, we showed that inclusion of MRE measurements in

statistical models helped predict perfusion, with stiffer tissue associated with lower perfusion values.

Supplementary information

Image processing

Perfusion images of the healthy subjects from ASL were analysed in the nordicICE (NordicNeuroLab AS, Bergen, Norway) software. This resulted in maps of cerebral blood flow (CBF) (**Fig. 1B**) quantified in units of ml/100 g/min, given by the formula (12):

$$CBF = \frac{6000 \cdot \lambda \cdot (SI_{control} - SI_{label}) \cdot e^{\frac{PLD}{T_{1,blood}}}}{2 \cdot \alpha \cdot T_{1,blood} \cdot SI_{PD} \cdot (1 - e^{-\frac{\tau}{T_{1,blood}}})} [ml/100g/min]$$

The following parameters were applied: $T_{1,blood}$= 1650 ms, labelling efficiency α of 0.85, and brain-blood water partition coefficient λ=0.9 ml/g (12). Motion correction and co-registration between the ASL and the proton density images were performed prior to analysis. Because ASL in general has low sensitivity for subtle perfusion levels in white matter (12), our study includes perfusion values from deep- and cortical gray matter regions only.

The DTI and DSC images were corrected for EPI-distortion effects prior to analysis using the geometric distortion correction method FSL TOPUP (11,31). Thereafter, diffusion tensor imaging analysis was performed in nordicICE with motion correction, automatic detection of noise threshold and noise level cutoff. The tissue diffusivity was measured by the apparent diffusion coefficient (ADC), and the tissue anisotropy was measured by the fractional anisotropy index (FA). Patient perfusion images were also analysed in nordicICE (32) utilizing both motion- and leakage-correction on DSC data. This produced map of cerebral blood flow normalized to white matter (nCBF), leakage, and vessel size index (VSI). The two latter maps were available for seven of the nine patients.

For the MRE, phase-unwrapping and pixel-wise temporal Fourier transformation were performed on the displacement phase data in order to obtain the tissue displacement in the frequency domain. The data was filtered in image space using an 11th order Blackmann Harris filter (33), before the curl operator was applied in the image to eliminate information originating from the compressional wave component (34). Through inversion, we then obtained maps of the shear storage modulus G′ (as a measure for stiffness) and the shear loss modulus G″ (related to the viscosity, meaning the tissue's ability to dissipate energy). To avoid artefacts from MRE reconstruction at the edge of the brain, elastography maps were eroded by 2 pixels. MRE data quality was assessed by degree of temporal nonlinearity in the MRE data, which is a measure of noise in the original phase data (29), and the ratio between the amplitude of the curl and the amplitude of the divergence (15). This ratio quantifies the signal (curl) to noise (divergence) since the divergence of the displacement is approximately zero due to the incompressible nature of tissue. All scans had a mean curl-divergence ratio above 5 and any voxels with nonlinearity above 50 % were excluded in the MRE maps.

Image registration and analysis

Segmentations of patient data

Segmentations of contrast-enhancing tumor, edema, necrosis, and normal-appearing gray and white matter was performed automatically using a convolutional neural network (CNN). This CNN is based on the 3D-Unet architecture defined by Juan-Albarracín et al. (35), trained with 262 BRATS (36,37) pre-surgical exams and 222 follow-up exams from our institution. The segmentations were done for each patient based on pre- and post-contrast $T1_w$, images, $T2_w$ and FLAIR images. Contrast-enhancing and necrotic tumor were defined as the enhancing and non-enhancing tumor region on post-contrast $T1_w$ images, respectively. Edema was defined as the hyperintense region on the FLAIR images. Gray- and white-matter masks were eroded by one voxel, and only the opposite hemisphere of the brain from the tumor was used for the normal-appearing gray- and white-matter masks. For the cases where the tumor affected both hemispheres, a 3 cm margin from the distal edge of the tumor and edema was used for the gray and white matter masks.

For comparisons between patients on an image voxel level, and for calculations of gradients outward from the patients, all maps were registered to the Montreal Neurological Institute (MNI) space (38), by means of an affine transformation and using a nearest-neighbour interpolation to preserve image voxel integrity. For the regression analysis on the voxel level, all maps were smoothed with a 3D Gaussian filter with sigma 1. The analysis was performed in Matlab (version R2021a, MathWorks, Natick, MA, USA).

To assess the spatial distribution of the parameters in necrosis, the distance to contrast-enhancing tumor was calculated for all points in the necrosis, and normalized to the maximum distance to contrast-enhancing tumor. This was repeated in contrast-enhancing tumor, using the distance to edema, and in edema, using the distance to normal-appearing tissue. For visualization, the gradients were smoothed using a Gaussian-weighted moving average filter of window length 70.

In order to make gradients outward from the lesion edge, here defined as the distal edema, an ROI consisting of necrosis, contrast-enhancing tumor and edema was dilated 1 mm at a time, 30 times. For each dilation, the last ROI was subtracted and the mean value of each new layer calculated. The gradients were smoothed using a Gaussian-weighted moving average filter of window length 10.

Regions of interest in healthy subjects

All image registrations in healthy subjects were performed using Matlab and SPM12 (version 7487, Wellcome Trust Centre for Neuroimaging, London). First, anatomical $T1_w$ images were warped to the MNI brain region template (39), and the inverse deformation fields were used to reorient the binary maps of the brain regions of interest into the each subject's anatomical space. T1 images and labels were then co-registered by affine transformations, using nearest-neighbour interpolation, into the native spaces of the MRE, DTI and the ASL images.

ROIs in the healthy subjects were extracted from the MNI template. The deep gray matter regions included in our study were head of the caudate nucleus, putamen, thalamus and hippocampus. The cortical gray matter regions included were the frontal lobe, the occipital lobe, the parietal lobe and the temporal lobe. For MRE and DTI images, a white matter ROI was also included. ADC maps from the diffusion acquisition was used to reduce any potential errors from partial volume effects. A mask with a cut-off ADC value of $< 1.2 \times 10^{-3}$ mm^2/s was used

to exclude voxels with free diffusion from DTI and MRE maps, to ensure no voxels with cerebrospinal fluid were included (40).

References

1. Stupp R, Mason WP, van den Bent MJ, et al. Radiotherapy plus concomitant and adjuvant temozolomide for glioblastoma. N Engl J Med 2005;352(10):987-996.
2. Wen PY, Macdonald DR, Reardon DA, et al. Updated response assessment criteria for high-grade gliomas: response assessment in neuro-oncology working group. J Clin Oncol 2010;28(11):1963-1972.
3. Pepin KM, Ehman RL, McGee KP. Magnetic resonance elastography (MRE) in cancer: Technique, analysis, and applications. Prog Nucl Magn Reson Spectrosc 2015;90-91:32-48.
4. Streitberger KJ, Reiss-Zimmermann M, Freimann FB, et al. High-resolution mechanical imaging of glioblastoma by multifrequency magnetic resonance elastography. PLoS One 2014;9(10):e110588.
5. Reiss-Zimmermann M, Streitberger KJ, Sack I, et al. High Resolution Imaging of Viscoelastic Properties of Intracranial Tumours by Multi-Frequency Magnetic Resonance Elastography. Clin Neuroradiol 2015;25(4):371-378.
6. Pepin KM, McGee KP, Arani A, et al. MR Elastography Analysis of Glioma Stiffness and IDH1-Mutation Status. AJNR Am J Neuroradiol 2018;39(1):31-36.
7. Streitberger KJ, Lilaj L, Schrank F, et al. How tissue fluidity influences brain tumor progression. Proc Natl Acad Sci U S A 2020;117(1):128-134.
8. Patel AP, Tirosh I, Trombetta JJ, et al. Single-cell RNA-seq highlights intratumoral heterogeneity in primary glioblastoma. Science 2014;344(6190):1396-1401.
9. D'Alessio A, Proietti G, Sica G, Scicchitano BM. Pathological and Molecular Features of Glioblastoma and Its Peritumoral Tissue. Cancers (Basel) 2019;11(4).
10. Digernes I, Bjornerud A, Vatnehol SAS, et al. A theoretical framework for determining cerebral vascular function and heterogeneity from dynamic susceptibility contrast MRI. J Cereb Blood Flow Metab 2017;37(6):2237-2248.
11. Andersson JL, Skare S, Ashburner J. How to correct susceptibility distortions in spin-echo echo-planar images: application to diffusion tensor imaging. Neuroimage 2003;20(2):870-888.
12. Alsop DC, Detre JA, Golay X, et al. Recommended implementation of arterial spin-labeled perfusion MRI for clinical applications: A consensus of the ISMRM perfusion study group and the European consortium for ASL in dementia. Magn Reson Med 2015;73(1):102-116.
13. Hiscox LV, Johnson CL, Barnhill E, et al. Magnetic resonance elastography (MRE) of the human brain: technique, findings and clinical applications. Phys Med Biol 2016;61(24):R401-R437.
14. Runge JH, Hoelzl SH, Sudakova J, et al. A novel magnetic resonance elastography transducer concept based on a rotational eccentric mass: preliminary experiences with the gravitational transducer. Phys Med Biol 2019;64(4):045007.
15. Svensson SF, De Arcos J, Darwish OI, et al. Robustness of MR Elastography in the Healthy Brain: Repeatability, Reliability, and Effect of Different Reconstruction Methods. J Magn Reson Imaging 2021.
16. Simon M, Guo J, Papazoglou S, et al. Non-invasive characterization of intracranial tumors by magnetic resonance elastography. New Journal of Physics 2013;15.
17. Riek K, Millward JM, Hamann I, et al. Magnetic resonance elastography reveals altered brain viscoelasticity in experimental autoimmune encephalomyelitis. Neuroimage Clin 2012;1(1):81-90.

18. Schregel K, Nazari N, Nowicki MO, et al. Characterization of glioblastoma in an orthotopic mouse model with magnetic resonance elastography. NMR Biomed 2018;31(10):e3840.
19. Carmeliet P, Jain RK. Angiogenesis in cancer and other diseases. Nature 2000;407(6801):249-257.
20. Latysheva A, Geier OM, Hope TR, et al. Diagnostic utility of Restriction Spectrum Imaging in the characterization of the peritumoral brain zone in glioblastoma: Analysis of overall and progression-free survival. Eur J Radiol 2020;132:109289.
21. Jain RK, Martin JD, Stylianopoulos T. The role of mechanical forces in tumor growth and therapy. Annu Rev Biomed Eng 2014;16:321-346.
22. Juge L, Doan BT, Seguin J, et al. Colon tumor growth and antivascular treatment in mice: complementary assessment with MR elastography and diffusion-weighted MR imaging. Radiology 2012;264(2):436-444.
23. Sack I, Beierbach B, Wuerfel J, et al. The impact of aging and gender on brain viscoelasticity. Neuroimage 2009;46(3):652-657.
24. Arani A, Murphy MC, Glaser KJ, et al. Measuring the effects of aging and sex on regional brain stiffness with MR elastography in healthy older adults. Neuroimage 2015;111:59-64.
25. Takamura T, Motosugi U, Sasaki Y, et al. Influence of Age on Global and Regional Brain Stiffness in Young and Middle-Aged Adults. J Magn Reson Imaging 2020;51(3):727-733.
26. Bunevicius A, Schregel K, Sinkus R, Golby A, Patz S. REVIEW: MR elastography of brain tumors. Neuroimage Clin 2019;25:102109.
27. Hiscox LV, McGarry MDJ, Schwarb H, et al. Standard-space atlas of the viscoelastic properties of the human brain. Hum Brain Mapp 2020;41(18):5282-5300.
28. Guo J, Hirsch S, Fehlner A, et al. Towards an elastographic atlas of brain anatomy. PLoS One 2013;8(8):e71807.
29. Yeung J, Juge L, Hatt A, Bilston LE. Paediatric brain tissue properties measured with magnetic resonance elastography. Biomech Model Mechanobiol 2019;18(5):1497-1505.
30. Green MA, Bilston LE, Sinkus R. In vivo brain viscoelastic properties measured by magnetic resonance elastography. NMR Biomed 2008;21(7):755-764.
31. Hovden IT, Geier OM, Digernes I, et al. The impact of EPI-based distortion correction of dynamic susceptibility contrast MRI on cerebral blood volume estimation in patients with glioblastoma. Eur J Radiol 2020;132:109278.
32. Bjornerud A, Emblem KE. A fully automated method for quantitative cerebral hemodynamic analysis using DSC-MRI. J Cereb Blood Flow Metab 2010;30(5):1066-1078.
33. Albrecht HH. A family of cosine-sum windows for high-resolution measurements. Volume 5: IEEE; 2001. p. 3081-3084 vol.3085.
34. Sinkus R, Tanter M, Xydeas T, Catheline S, Bercoff J, Fink M. Viscoelastic shear properties of in vivo breast lesions measured by MR elastography. Magn Reson Imaging 2005;23(2):159-165.
35. Juan-Albarracin J, Fuster-Garcia E, Garcia-Ferrando GA, Garcia-Gomez JM. ONCOhabitats: A system for glioblastoma heterogeneity assessment through MRI. Int J Med Inform 2019;128:53-61.
36. Menze BH, Jakab A, Bauer S, et al. The Multimodal Brain Tumor Image Segmentation Benchmark (BRATS). IEEE Trans Med Imaging 2015;34(10):1993-2024.
37. Bakas S, Akbari H, Sotiras A, et al. Advancing The Cancer Genome Atlas glioma MRI collections with expert segmentation labels and radiomic features. Sci Data 2017;4:170117.
38. Brett M, Johnsrude IS, Owen AM. The problem of functional localization in the human brain. Nat Rev Neurosci 2002;3(3):243-249.
39. Tzourio-Mazoyer N, Landeau B, Papathanassiou D, et al. Automated anatomical labeling of activations in SPM using a macroscopic anatomical parcellation of the MNI MRI single-subject brain. Neuroimage 2002;15(1):273-289.

40. Bykowski JL, Latour LL, Warach S. More accurate identification of reversible ischemic injury in human stroke by cerebrospinal fluid suppressed diffusion-weighted imaging. Stroke 2004;35(5):1100-1106.